Lunar far side positioning enabled by a CubeSat system deployed in an Earth-Moon halo orbit

Hongru Chen, Jiangkai Liu, Long Long, Zhenyu Xu, Yazhe Meng, Hao Zhang

Lunar Far Side Positioning enabled by a CubeSat System deployed in an Earth-Moon Halo Orbit[☆]

Hongru Chen[a,1,2,*], Jiangkai Liu, Long Long, Zhenyu Xu, Yazhe Meng[b,1,3],
Hao Zhang[b,1]

[a]*77 Av. Denfert-Rochereau, 75014 Paris, France*
[b]*9 Dengzhuang S Rd., 100094 Beijing, China*

Abstract

For explorations of the far side of the Moon, it is necessary to tackle the challenge of navigation and communication as the far side is invisible to the Earth. This paper proposes a low-cost mission concept that consists of four CubeSats in an Earth-Moon L_2 (EML2) halo orbit. The mission objective is to provide real-time positioning service for lunar far-side assets, taking advantage of the visibility of EML2 halo orbits to both the Earth and lunar far side. Being miniature, CubeSats can be carried by a mother spacecraft and deployed during the mid-course. As CubeSat missions are generally constrained by limited communication, power, and propulsion capacities, this paper presents a feasibility study that takes into account the high-fidelity dynamical environment and system constraints. This paper analyzes the positioning performance in terms of accuracy, and spatial and temporal coverage. In addition, the requirement of deployment in terms of Δv budget and thrust magnitude is also investigated. Results show that 1) a positioning accuracy of 2.7 km is achievable; and 2) several state-of-the-art propulsion systems can meet the requirement of deployment and the stationkeeping for an acceptable duration.

---

[*]Corresponding author
Email addresses: hongru.chen@hotmail.com (Hongru Chen),
kai.ljk@hotmail.com (Jiangkai Liu, Long Long, Zhenyu Xu, Yazhe Meng),
hao.zhang.zhr@gmail.com (Hao Zhang)
[1]Key Laboratory of Space Utilization, Technology and Engineering Center for Space Utilization, Chinese Academy of Sciences
[2]IMCCE, Observatoire de Paris, Université PSL, CNRS
[3]University of Chinese Academy of Sciences

1. Introduction

CubeSats are miniature spacecraft that can take advantage of piggyback launch opportunities. By deploying them into space, multiple mission objectives and cooperative operations can be achieved. For instance, the Exploration Mission 1 has selected 13 CubeSats as secondary payloads (NASA (2015)). The selected OMOTENASHI (Hernando-ayuso et al. (2017); Campagnola et al. (2018)), EQUULEUS (Oshima et al. (2017); Oguri et al. (2017)), Lunar Flashlight (Lai et al. (2018)), NEA Scout (Frick et al. (2014), etc., are planned to achieve a wide range of science and technology objectives, such as semi-hard landing on the Moon, lunar water observation, solar sail demonstration, asteroid flyby, etc. Two CubeSats MarCo were launched with the Martian lander InSight, and were planned to provide communication relay during the landing phase of InSight (Klesh (2014)). The Asteroid Impact Mission is planned to rendezvous with the binary asteroid 65803 Didymos and deploy a lander and multiple CubeSats to establish inter-satellite network (Kuppers et al. (2015)). Multiple satellites together can perform cooperative operations, such as geolocation (Gurfil et al. (2012)) and autonomous navigation via inter-satellite ranging (Hill and Born (2007)). This paper presents a CubeSat constellation for positioning landers or rovers on the far side of the Moon.

The terrain and resources on the far side of the Moon are very different from those on the near side, and hence worth exploring. In addition, the far side is an ideal platform for radio astronomy as the Moon can shield the radio noise from the Earth. There are several ongoing and planned missions to explore the far side of the Moon (e.g. Burns et al. (2013)). A CubeSat mission LUMIO is planned to observe meteoroid impacts on the far side of the Moon (Speretta et al. (2018); Cipriano et al. (2018); Franzese et al. (2019)). Landers and rovers can perform effective in-situ observation. China has recently landed the Chang′E-4 lander on the far side (Li et al. (2014)). On the other hand, as the far side is invisible to the Earth, challenges for navigation and communication arise for Lunar far-side missions. Moreover, because the far-side terrain is rougher than the near-side, the requirement of landing accuracy is stricter. Hill and Born (2007) and Hesar et al. (2015)

2

have studied tracking satellites in an Earth-Moon L_2 (EML2) halo orbit and assets on the far side of the Moon using the inter-satellite tracking technique LiAISON. However, LiAISON is not capable of real-time positioning of maneuvering objects, such as a Lunar lander. Similar to the GPS technique, at least four tracking stations are required for real-time positioning. In addition, the problem of distributing multiple elements into a favourable tracking geometry has not been well addressed. To that end, this paper proposes employing four CubeSats in an EML2 halo orbit to assist the positioning of the lunar far-side lander, and addresses the requirement of deployment (see also Chen et al. (2017, 2018b)).

Being equipped with micro subsystems, CubeSats have clear limitations on their communication, power, and orbital maneuver capacities, which constrain the mission design. Hence, it is of interest to explore CubeSat applications with state-of-the-art technologies. Tardivel et al. (2017) have assessed the possibility of nanospacecraft interplanetary trajectories considering technological conditions. This paper presents a feasibility study for the proposed CubeSat positioning mission, taking into account the high-fidelity dynamical environment, and system constraints and specifications. To support the required measurement operation, system design is briefly addressed in Section 2.2. The mission performance in terms of the positioning accuracy, and spatial and temporal coverage of the lunar surface are analyzed in Section 3. An extended application of the CubeSat constellation to the orbit determination of lunar orbiters is discussed in Section 4. As the four CubeSats should be distributed along the halo orbit to have a favorable geometry for positioning, the deployment trajectory is designed and optimized. The obtained relationship between the Δv budget and thrust magnitude is used to find suitable propulsion system models (See Section 5.1). The feasibility of using low thrusts in the deployment trajectory is specifically discussed. The staionkeeping simulation is performed to examine the mission lifetime (See Section 5.2).

2. Background

2.1. Mission orbit: Earth-Moon L_2 halo orbit

The dynamical environment of the Earth-Moon system can be approximated by the circular restricted three-body problem (CR3BP)(for details, see Szebehely (1967)). In the CR3BP, there are five equilibrium points where relative acceleration and velocity to the Earth-Moon rotating frame are zero.
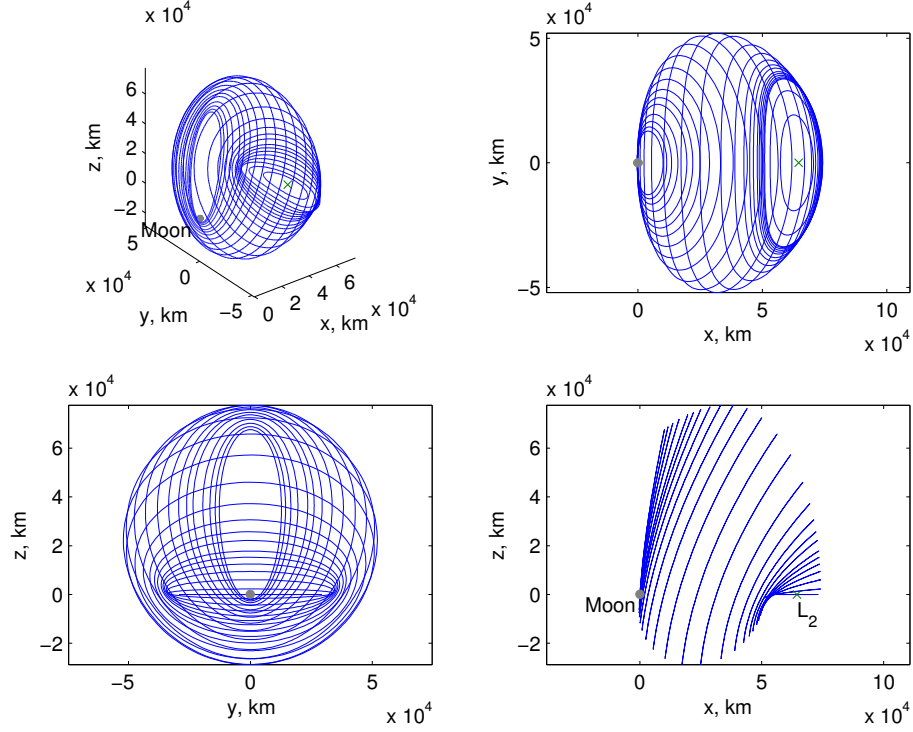
Figure 1: Earth-Moon L_2 halo orbits.

They are termed libration points or Lagrangian points labeled as L_1, L_2,..., L_5. The halo orbit is a three-dimensional periodic orbit about one of the co-linear points, L_1, L_2, and L_3. A halo orbit can be computed using a numerical differential correction constrained by the symmetry about the x-z plane in the rotating frame (for details, see Howell (1984)). A family of halo orbits can be obtained using the pseudo-arc-length continuation method (for details, see Doedel et al. (2003)). Figure 1 shows the family of northern EML2 halo orbits in the Moon-centered rotating frame.

The Earth-Moon L_2 (EML2) point is 64,500 km from the Moon on the far side. Halo orbits around EML2 are visible to both the Earth and far side of the Moon. Moreover, as the lines of sight to the Earth and the Moon are almost aligned, the communication operation and attitude control are relatively simple. Therefore, it is desirable to place four CubeSats in an EML2 halo orbit to support the positioning of assets on the far side of the Moon, such as a lander or rover (see Figure 2). In addition to the positioning service, such a system can be utilized to enhance the orbit determination of
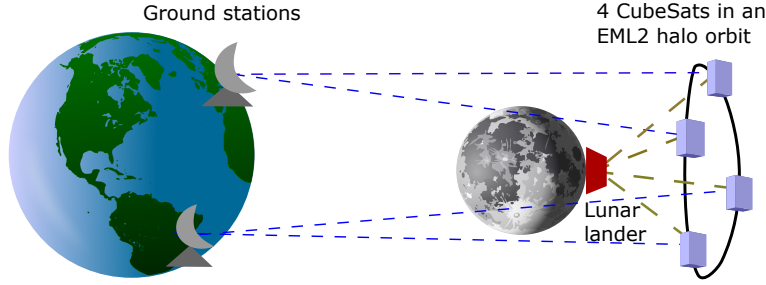
4

Figure 2: Schematic of tracking CubeSats and landers on the far side of the Moon.

lunar orbiters. Moreover, this system can transfer the status data of the lunar lander and the observation data of the Moon to ground stations.

2.2. Operation scheme and preliminary system design

To provide the desired positioning service, orbits of CubeSats are assumed to be determined through measurements from ground stations on the Earth. The CubeSats broadcast their ephemerides and time. Through ranging with the CubeSats, the lander can resolve its position. Therefore, payloads of the CubeSat are basically the communication system, which is capable of ranging and Doppler measurement, and a highly-stable atomic clock.

Components of a CubeSat are selected as listed in Table 1. A 3U (or 6U) frame is assumed with a space of 1U (or 4U) left for the propulsion system. A mass margin of 600 g is reserved to cover small electrical and mechanical parts, the reaction control thrusters used for reaction wheel unloading (if not included in the propulsion system), radiation shields, etc. The mass of the CubeSat without a propulsion system is around 4.2 kg for a 3U setting, or 4.7 kg for a 6U setting. The 3U configuration of the CubeSat is displayed in Figure 3.

Considering the limited power of the CubeSat, during the standby mode, the CubeSat panel with solar arrays is pointed to the Sun. The solar panel when pointed to the Sun can generate a power of 33 W. During this mode, the CubeSat can charge the battery and receive telecommands from the Earth or the Moon via its omnidirectional UHF antenna set at a low power consumption. When a ground station or a lunar user requests ranging with the CubeSats, the CubeSats switch to the operating mode, during which the CubeSats transmit ranging codes via their S-band high-gain antennas at a power consumption of 20 W. The experience of the ARTEMIS mission shows

5

that a tracking pass of 1 hour twice per day can lead to satisfactory accuracy of the orbit determination of the spacecraft around the EML2 point (Woodard et al. (2012)). The positioning for landing lasts around 12 min. The orbit determination of lunar orbiters takes 30 min to converge, as presented in Section 4. Hence, the capacity of the selected battery (i.e. 77 Wh) is considered sufficient for those short operations.

The link budget is computed based on Larson and Wertz (2005) considering specifications of the selected S-band transponder and antenna. As the downlink channel is generally much more constrained than the uplink, only the link budget of the downlink channel is considered here. The link budget analysis is presented in Table 2. It is shown that link budget is sufficient for the current communication and measurement settings. The measurement is discussed in the following subsection.

2.3. Measurement errors

It is assumed that the lunar user has a GNSS receiver. The user-equivalent range error (UERE) is mainly due to the thermal noise of the receiver, and the clock drift and ephemeris error of the CubeSats. The thermal noise in the receiver delay lock loop (DLL) and frequency lock loop (FLL) affect the pseudo-range and range rate measurements, respectively. The corresponding 1σ uncertainty, $\sigma_{\rho DLL}$ and $\sigma_{\dot{\rho} FLL}$, can be computed from (for details, see Kaplan and Hegarty (2006))

$$\sigma_{\rho DLL} = \lambda_c \sqrt{\frac{B_n}{2C/N_0} \frac{1}{B_{fe} T_c} \left[1 + \frac{1}{TC/N_0} \right]} \tag{1}$$

$$\sigma_{\dot{\rho} FLL} = \frac{\lambda_L}{2\pi T} \sqrt{\frac{4 B_n}{C/N_0} \left[1 + \frac{1}{TC/N_0} \right]} \tag{2}$$

where λ_c is the wavelength of ranging code chip, λ_L is the carrier wavelength, B_n the code loop noise bandwidth, B_{fe} is the double-sided front-end bandwidth, T is the prediction integration time, T_c is the chip period, and C/N_0 is the received carrier-to-noise density. Here, $\lambda_c = c/R_c$, in which R_c is the ranging chip-rate and c is the speed of light; and $\lambda_L = c/f$, in which f is the signal frequency. Assuming using the Gold code chip whose length is 1023 chips, $T_c = \lambda_c/c \times 1023$. In addition, $B_n = 0.5$ Hz, $B_{fe} = 2 \times R_c$, and $T = 1$ s are used in this work; and λ_L, R_c and C/N_0 are determined in the link budget analysis. Table 2 also shows the corresponding $\sigma_{\rho DLL}$ and $\sigma_{\dot{\rho} FLL}$.

6

Table 1: Components of the CubeSat (without a propulsion system)

Subsystems	Components	Weight, g	Size, mm³	Power, W
Structure[1]	1 3(or 6)U frame	600(or 1100)	100×100(or 200)×300	/
	2 deployable panels	440	150×300×10 (each)	/
Power	14 solar arrays[2]	700	82.5×98×2.4 (each)	+33 (Sun-pointing)
	1 battery[3]	500	93×86×41	+77 h
ADCS	4 reaction wheels[1]	220	25×50×55	-0.8
	1 star tracker[4]	170	50×50×47	-1.5
	1 MEMS IMU[5]	20	20×20×15	-0.6
	4 Sun sensors[6]	20	27.4×14×5.9 (each)	-0.33
Communication	4 UHF antennas[7]	16.5	70×70×14	/
	1 UHF/VHF transceiver[8]	85	90×96×15	-0.2
	4 S-band patch antennas[9]	256	98×98×5.5 (each)	/
	1 S-band transponder[10]	370	98×98×50	-20
C&DH	1 on-board computer[11]	100	96×90×12.4	-0.4
Payload	1 atomic clock[12]	85	18.3×50.8×50.8	-8
Margin	/	600	/	-2
Total	/	4183(or 4683)	/	-14 (standby) -34 (operating)

[1] Based on the experience of CubeSat structure development (see Long et al. (2017); Yang et al. (2019)).
[2] DHV-CS-10, https://www.cubesatshop.com/product/cubesat-solar-panels/, accessed 19-Nov-2018.
[3] GOMspace NanoPower BPX, https://gomspace.com/UserFiles/Subsystems/datasheet/gs-ds-nanopower-bpx-3-18.pdf, accessed 19-Nov-2018.
[4] MAI-SS Space Sextant, https://www.cubesatshop.com/product/mai-ss-space-sextant/, accessed 19-Nov-2018.
[5] Micro Aerospace MASIMU02 http://www.micro-a.net/imu-tmpl.html, accessed 19-Nov-2018.
[6] NanoSSOC-A60 https://www.cubesatshop.com/product/nano-ssoc-a60-analog-sun-sensor/, accessed 19-Nov-2018.
[7] Nano Avionics https://n-avionics.com/subsystems/cubesat-uhf-antenna/, accessed 19-Nov-2018.
[8] ISIS https://www.isispace.nl/product/vhf-downlink-uhf-uplink-full-duplex-transceiver/, accessed 19-Nov-2018.
[9] Endurosat https://www.endurosat.com/products/cubesat-s-band-patch-antenna/, accessed 19-Nov-2018.
[10] Vulcan, information based on Schaire (2017).
[11] ISIS, https://www.cubesatshop.com/product/isis-on-board-computer/, accessed 19-Nov-2018.
[12] Microsemi SA.35, https://www.microsemi.com/product-directory/embedded-clocks-frequency-references/3825-miniature-atomic-clock-mac#resources, accessed 19-Nov-2018. Note that as this product is not space-qualified, mass and volume margins are reserved for the clock. However, the aging value of the SA.35 is be adopted as a reference number for this project.
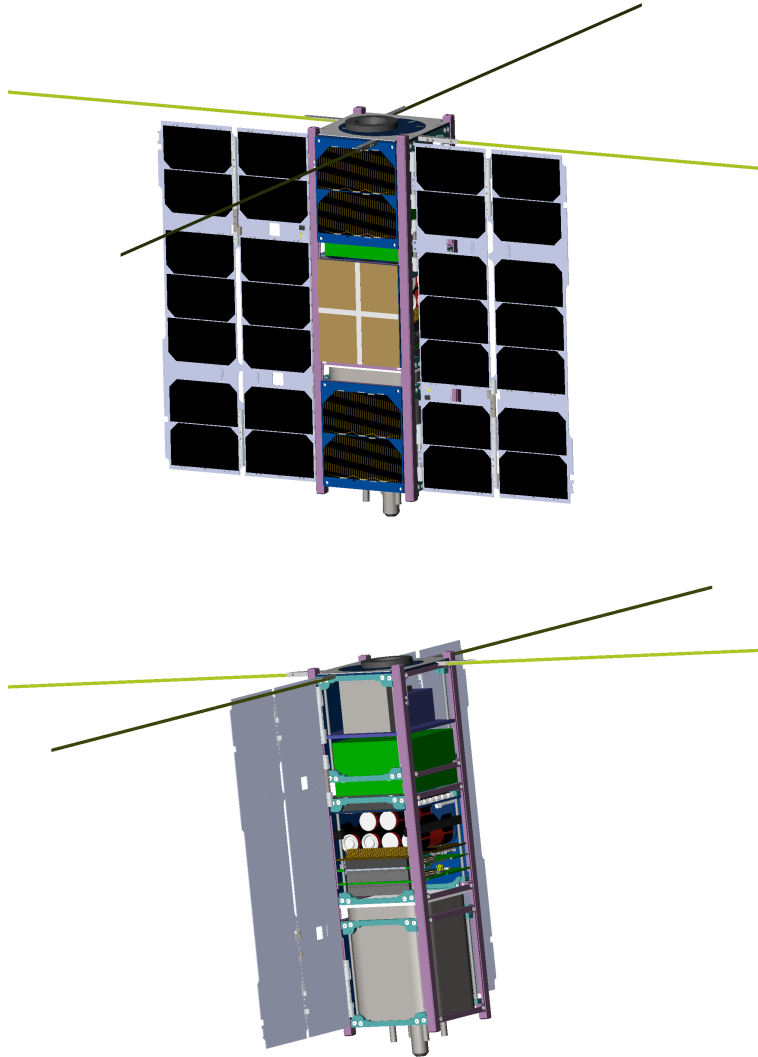
Figure 3: Outer and inner configuration of the CubeSat.

Table 2: Link budgets, $\sigma_{\rho DLL}$, and $\sigma_{\dot{\rho} FLL}$

Item	Symbol	Units	To Moon	To Earth
Frequency	f	MHz	2425	2200
Transmitter output power[1]	P	Watts	4	4
Transmitter output power	P	dBW	6.02	6.02
Transmit antenna gain[2]	G_t	dB	8.3	8.3
Equiv. isotropic radiated power	$EIRP$	dBW	14.32	14.32
Propagation path length	S	km	5.12×10^4	4.5×10^5
Space loss	L_s	dB	-194.33	-212.36
Atmospheric attenuation	L_a	dB	0	-0.3
Receive antenna diameter	D_r	m	0.04	35
Helix antenna length	L	m	0.42	/
Peak receive antenna gain	G_{rp}	dBi	15.74	55.54
Receive antenna beamwidth	θ_r	deg	27.78	0.27
Maximum receive antenna pointing error	e_{rmax}	deg	16.65	0.2
Receive antenna pointing loss	Lpr	dB	-4.31	-6.45
Receive antenna gain	G_r	dBi	11.43	49.09
Received power	C	dB	-168.57	-149.25
System noise temperature	T_s	K	135	135
Data rate	R	bps	1200	30000
E_b/N_0	E_b/N_0	dB	4.92	10.26
Required E_b/N_0	Req E_b/N_0	dB	4	4
Margin	/	dB	0.92	6.26
C/N_0	C/N_0	dB	38.72	/
C/N_0	C/N_0	kHz	7.45	/
Chip rate	R_c	bps	1000	/
Chip length	λ_c	km	290.35	/
Chip period	T_c	s	1.023	/
Carrier Wavelength	λ_L	m	0.12	/
Maximum $\sigma_{\rho DLL}$	$\sigma_{\rho DLLmax}$	m	52.6	/
Minimum $\sigma_{\rho DLL}$[3]	$\sigma_{\rho DLLmin}$	m	32.01	/
Maximum $\sigma_{\dot{\rho} FLL}$	$\sigma_{\dot{\rho} FLLmax}$	m/s	0.02	/
Minimum $\sigma_{\dot{\rho} FLL}$[3]	$\sigma_{\dot{\rho} FLLmin}$	m/s	0.01	/

[1] Vulcan S-band transponder

[2] Endurosat S-band patch antenna

[3] When $e_r = 0$

It is assumed that a desired probability of bit error $BER = 1 \times 10^{-6}$ can be achieved at a ratio of energy-per-bit to noise density $E_b/N_0 = 4$ dB, using the BPSK coding (i.e. R $^1/_2$ Viterbi $K = 7$ RS(255,223)). E_b/N_0 is mainly influenced by the space loss, L_s, and the receive antenna pointing loss, L_{pr}. L_s and L_{pr} depend on the chosen halo orbit and signal frequency. The geometry and coverage analysis in Section 3.1 and Section 3.2 reveals that a small halo orbit with z-amplitude $A_z = 15,000$ km and y-amplitude $A_y = 35,000$ km is favorable. To cover this halo orbit from the lunar surface, the antenna pointing error, e_r, can be up to 32.6°. Assuming that four helix S-band antennas are mounted on the user to target four partitioned segments of the halo orbit, respectively, the maximum e_r is reduced to 16.65°. In this case, $\sigma_{\rho DLL}$ ranges from 32 m to 53 m, and $\sigma_{\dot{\rho} FLL}$ ranges from 1 cm/s to 2 cm/s. Note that e_r as well as L_{pr}, $\sigma_{\rho DLL}$, and $\sigma_{\dot{\rho} FLL}$ can be further reduced with more dedicated antennas mounted on the lunar user.

It is assumed that the orbit determination of the CubeSats can achieve an accuracy that the EML2 mission ARTEMIS achieved. According to the operational result of ARTEMIS (Woodard et al. (2012)), the initial 3σ uncertainties for position and velocity are 1 km and 1cm/s, respectively. Using a Kalman filter and recursive smoother methods, uncertainties of 185 m and 0.06 cm/s can be provided across stationkeeping maneuver events. By processing a 10-day batch tracking data, uncertainties of 20 m and 0.002 cm/s are achievable.

Another error source of ranging is the clock drift onboard the CubeSats. The chosen Microsemi SA.35 clock has a stability of 2.5×10^{-11} after 1 day of operation. Assuming that the orbit and clock determination of the CubeSats are performed twice per day, the clock uncertainty after half a day is 1 μs, resulting in a ranging uncertainty, $\sigma_{\rho clock}$, of 300 m. The CubeSat clock drift contributes the major part of ranging errors.

3. Positioning Performance

3.1. Geometric effect

Besides measurement errors, the positioning accuracy is associated with the geometry of reference points. The measurement data is the pseudo-range, ρ. The pseudo-range ρ_i between the user and the i-th CubeSat is expressed as,

$$\rho_i = \sqrt{(x - x_i)^2 + (y - y_i)^2 + (z - z_i)^2} + c\Delta t_{clock} + \Delta\rho_{clock} + \Delta\rho_{DLL} \quad (3)$$

where x, y and z denote the position coordinates of the user, x_i, y_i and z_i denote the position coordinates of the i-th CubeSat, Δt_{clock} denotes the clock error of the user, and $\Delta \rho_{clock}$ and $\Delta \rho_{DLL}$ denote the measurement error due to the clock drift of the CubeSat and the thermal noise in the receiver, respectively. Real-time x, y, z, and Δt_{clock} can be resolved with at least four simultaneous ρ_i known (see also Vallado (2007); Kaplan and Hegarty (2006)).

$\Delta \rho_{clock}$, $\Delta \rho_{DLL}$, and the error of CubeSat positions, ΔR_{sat}, will lead to errors in the solution. The uncertainty of CubeSat position is assumed isotropic; that is, the uncertainty of each component $\sigma(\Delta x_i) = \sigma(\Delta R_{sat})/\sqrt{3}$. The position uncertainty of the lunar user can be expressed as,

$$\sigma(\Delta R_{usr}) = PDOP \times \sigma_{UERE} \tag{4}$$

where the range uncertainty σ_{UERE} is the RSS of $\sigma_{\rho clock}$, $\sigma_{\rho DLL}$, and $\sigma(\Delta x_i)$. $PDOP$ can be computed from (for details, see Kaplan and Hegarty (2006)),

$$\mathbf{P} = \begin{bmatrix} \frac{(x_1-x)}{R_1} & \frac{(y_1-y)}{R_1} & \frac{(z_1-z)}{R_1} & 1 \\ \frac{(x_2-x)}{R_2} & \frac{(y_2-y)}{R_2} & \frac{(z_2-z)}{R_3} & 1 \\ \frac{(x_3-x)}{R_3} & \frac{(y_3-y)}{R_3} & \frac{(z_3-z)}{R_3} & 1 \\ \frac{(x_4-x)}{R_4} & \frac{(y_4-y)}{R_4} & \frac{(z_4-z)}{R_4} & 1 \end{bmatrix} \tag{5}$$

$$\mathbf{D} = \left(\mathbf{P}^T \mathbf{P}\right)^{-1} \tag{6}$$

and

$$\text{PDOP} = \sqrt{d_{11} + d_{22} + d_{33}} \tag{7}$$

where d_{ij} denotes the element in the i-th row and j-th column of matrix $\mathbf{D}$. The smaller $PDOP$ is, the better the geometry is for positioning. The form of Eq.(4) also applies to the velocity determination of the lunar user with range rate information available.

The constellation of the four CubeSats can be defined by A_z of the halo orbit and the difference of the phase angle, $\Delta\phi$, between two neighboring CubeSats. Figure 4 shows four different constellations and the corresponding $PDOP$ during one halo period. Here, $PDOP$ is computed at the center of the Moon, as the position on the surface of the far side barely influences the result. $PDOP$ goes extremely high when the angular separation of the four CubeSats is narrow as viewed from the Moon. The poor geometry appears when two CubeSats are in the north and the other two in the south of the halo orbit. $PDOP$ reaches the lowest point when the four CubeSats are separated

most widely. At that time, four CubeSats are roughly at the north, south, east, and west ends, respectively. Figure 4 only displays the part where $PDOP < 50$. It can be easily understood that the best constellation is with four CubeSats distributed evenly throughout the halo orbit with $\Delta\phi = 90°$. The overall $PDOP$ for $\Delta\phi = 90°$ is smaller than the overall $PDOP$ for $\Delta\phi = 60°$. In addition, $PDOP$ does not vary much with A_z when A_z is small. For a small A_z (i.e. $< 50{,}000$ km) and $\Delta\phi = 90°$, the minimum $PDOP$ is around 8.8. The overall $PDOP$ starts to degrade as A_z is further increased. $PDOP$ for $A_z = 77{,}000$ km exhibits an evident degradation. Therefore, small halo orbits near L_2 are favorable in terms of $PDOP$.

3.1.1. Simulation results

The constellation with $A_z = 15{,}000$ km and $\Delta\phi = 90°$ is used for further assessment. According to the analysis in Section 2.3, $\sigma_{\rho clock}$ is 300 m, and $\sigma_{\rho DLL}$ varies between 32 m and 53 m as the CubeSats move along the halo orbit. Here, $3\sigma(\Delta R_{sat}) = 1$ km and $3\sigma(\Delta R_{sat}) = 200$ m from results of the ARTEMIS operation are used for the worst and normal situations, respectively.

A Monte Carlo simulation is performed with given uncertainty quantities. Coordinates of the user at each tracking instance are resolved and compared to truth ones. The user position error ΔR_{usr} is shown in Figure 5. Only the lower parts of ΔR_{usr} are displayed, as at the "near-singular" geometry the poor $PDOP$ leads to very high errors. ΔR_{usr} essentially follows the variation of $PDOP$. Supposing that $3\sigma(\Delta R_{sat}) = 200$ m and a $\sigma(\Delta R_{usr})$ of 5 km is desired, a landing window lasts 2.5 days, and the waiting time is not longer than 1.2 days, which is acceptable for a lunar mission. Furthermore, as the duration of landing is only around 12 min, the lander can wait till $PDOP$ drops to the lowest level to perform landing. The lowest $PDOP$ repeats every quarter period, i.e. 3.7 days. The lowest ΔR_{usr} at the lowest $PDOP$ are 3 km and 2.7 km for the worst and normal situations, respectively.

3.2. Coverage of lunar surface

On the other hand, the positioning accuracy revealed in previous subsections does not apply to everywhere on the far side of the lunar surface. Due to the orbital movement of CubeSats and the spherical shape of the Moon, in some areas not all CubeSats are visible all the time. The lunar surface coverage enabled by constellations with $\Delta\phi = 90°$ and different A_z is shown in Figure 6. It can be seen that a small halo orbit has a broader converge
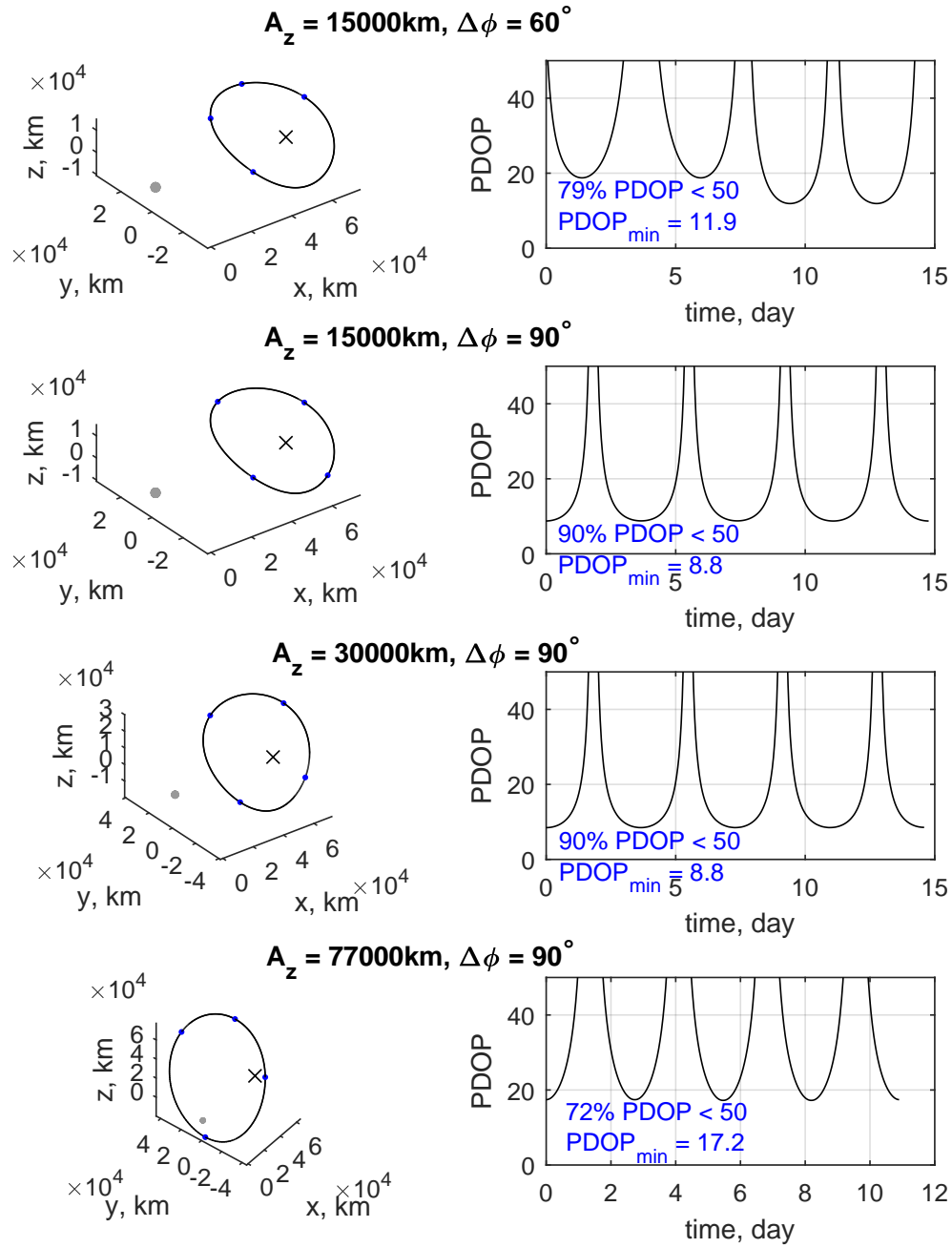
12

A$_z$ = 15000km, $\Delta\phi$ = 60°

79% PDOP < 50
PDOP$_{min}$ = 11.9

A$_z$ = 15000km, $\Delta\phi$ = 90°

90% PDOP < 50
PDOP$_{min}$ = 8.8

A$_z$ = 30000km, $\Delta\phi$ = 90°

90% PDOP < 50
PDOP$_{min}$ = 8.8

A$_z$ = 77000km, $\Delta\phi$ = 90°

72% PDOP < 50
PDOP$_{min}$ = 17.2

Figure 4: PDOP for different constellations.
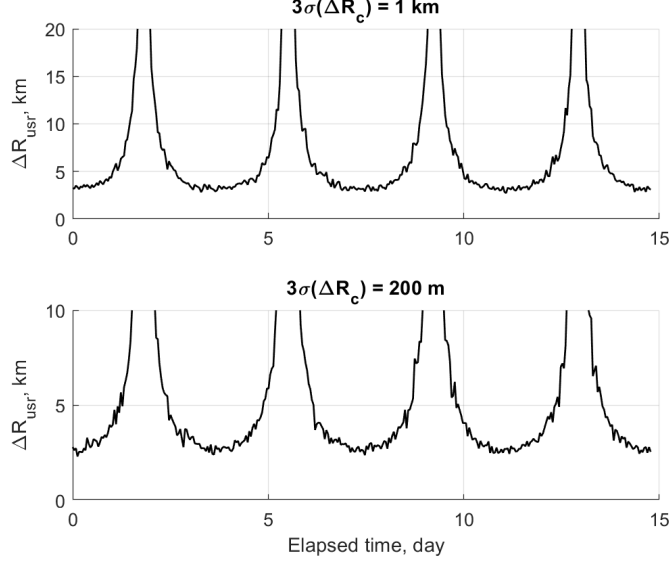
Figure 5: Results of positioning simulation.

than a larger halo orbit. For $A_z = 15{,}000$ km, the far-side area with longitude between [E125°, W125°] and latitude between [N75°, S75°] is covered. The interesting South Pole-Aitken basin is within the covered area. The halo orbit with $A_z = 77{,}000$ km is a near rectilinear halo orbit (NRHO). While the NRHO is more stable than a halo orbit near L_2 (Zimovan et al. (2017); Davis et al. (2017)), it is shown unsuitable for the proposed mission regarding positioning accuracy and simultaneous coverage.

4. Orbit Determination of Lunar Orbiters

Although the present CubeSat constellation is aimed for the positioning of landers and rovers on the far side of the Moon, it can be used for the orbit determination of low-lunar-orbit (LLO) satellites as well. In particular, near real-time orbit determination of LLO can be achieved.

It is assumed that LLO satellite has a GNSS-like receiver, and the orbit determination of an LLO satellite is based on the ranging and Doppler measurements with the CubeSat constellation. The measurement data is received every 10 seconds. The filter is Extended-Karlman-Filter (EKF) based. For the simulation, the LLO satellite is assumed in a near-circular orbit about the Moon with an inclination of 6° and an altitude of 150 km. The "truth"
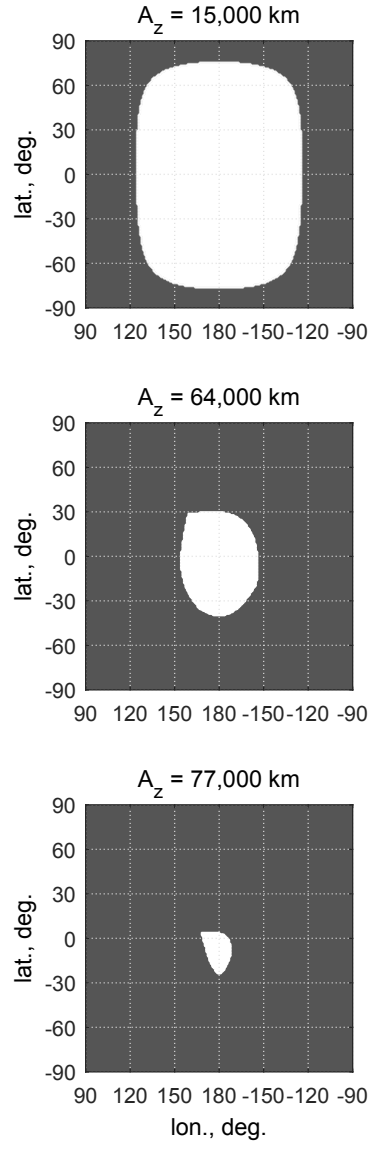
14

Figure 6: The coverage (white area) of the far side of lunar surface.

Table 3: Dynamical model settings

Items	Truth	Filter
Non-Spherical Lunar Gravity Model	20×20 GRGM	13×13 GRGM
Solar Radiation Pressure	Spherical model, $C_R = 1.3$, area = 0.7 m^2	Spherical model, $C_R = 1.3$, area = 0.77 m^2
Integrator	7(8) Variable Step Runge-Kutta	4th Order Fixed Step Runge-Kutta
Integration Stepsize	1 second	10 seconds

orbit is produced by a high-fidelity propagator, whereas the filter adopts a medium-fidelity dynamical model. Table 3 lists the parameters used by both models. Note that the uncertainty of solar radiation pressure is set 10% in both models. Measurement data are generated by adding white noises to the range and range rate between the CubeSats and the lunar orbiter. The 1σ range uncertainty is the RSS of $\sigma_{\rho clock}$ and $\sigma_{\rho DLL}$. The magnitude of Doppler noises adopts the value of $\sigma_{\dot{\rho}FLL}$, which is 2 cm/s (see Table 2). Ephemerides of the CubeSats used in the filter are generated by adding white noise to each component of truth states. Here, the standard deviations are 192 m and 0.19 cm/s for position and velocity components, respectively, corresponding to the initial 3σ position uncertainty of 1 km and velocity of 1 cm/s, as mentioned in Section 2.3. The shadow of the Moon is also taken into account. The receiver clock offset is assumed constant and modeled by a random walk process. To construct the noise spectral density of the process, the process noise magnitude, $\sigma_{c\delta t_r}$, is set to be 500 m, and the auto-correlation time scale, $\tau_{c\delta t_r}$, of 100 s are used , which apply to a general GNSS receiver clock (Remco (2006)).

The measurement data are then processed by the filter to resolve the position and velocity of the satellite as well as the clock offset of the receiver. It is worthy mentioning that after the measurement update of the filter, a constant symmetric process noise covariance matrix $\mathbf{Q}$ is adopted to absorb

model errors. The value of $\mathbf{Q}$ is computed by

$$\mathbf{Q} = \left[\begin{array}{cc} \frac{1}{3}\Delta t^3 & \frac{1}{2}\Delta t^2 \\ \frac{1}{2}\Delta t^2 & \Delta t \end{array} \right] \otimes \mathbf{Q_w} \tag{8}$$

where Δt is the signal interval, $\otimes$ is the Kronecker product, and $\mathbf{Q_w}$ is a diagonal covariance matrix determined by the difference between the aforementioned two dynamical models. Here, the entries of $\mathbf{Q}$ are on an order of 10^{-5} to 10^{-6}.

The estimation process starts with initial position uncertainty of 10 km and velocity uncertainty of 10 m/s in each direction. Resolved position and velocity are then compared with truth states. The errors in the along-track, radial, and cross-track directions are shown in Figure 7. Number of visible CubeSats is also displayed in the figure. It can be observed that the estimation converges after about 30 min of signal-tracking. The achieved RSS errors of position and velocity are 15.4 m and 2.5 cm/s, respectively. The errors remain low for about one hour until the number of visible CubeSats decreases to one. Contacting with only one CubeSat is deficient for orbit determination, as the ranging uncertainty is quite large (i.e. equivalent to 360 m). Uncertainties of position and velocity in this case are 85 m and 10 cm/s, respectively. In the simulation, it is also noticed that the Doppler measurement significantly contributes to the convergence. In the absence of Doppler measurements, the filter can take as long as 2 hours to reach a convergence, which is unacceptable considering the limited operation duration due to the limited power capacity of the CubeSat.

To inspect the influence of the CubeSat geometry on navigation performance, another simulations starting at different epochs are carried out. Eight start epochs are sampled evenly during one period of the halo orbit (i.e. 15 days), which covers the best and the worst initial geometries (i.e. $PDOP$). Other simulation conditions remain the same. The results are not very different from the result shown in Figure 7. It can be concluded from the simulation results that the mean position accuracy is 16.1 m with a standard deviation of 1.26 m, and the mean velocity accuracy is 1.9 cm/s with a standard deviation of 0.53 cm/s, which proves the robustness of the system performance.
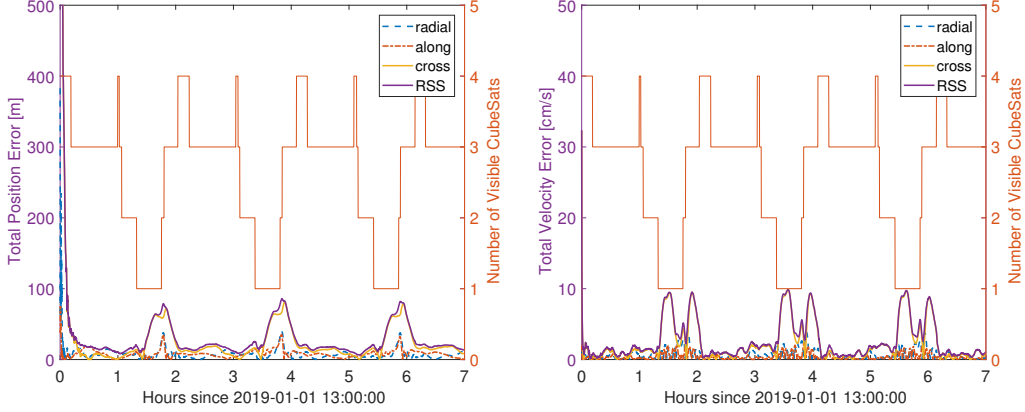
Figure 7: Navigation position (left) and velocity (right) error and the number of visible Cubesats as a function of elapsed time.

5. Trajectories and propulsion system sizing

Trajectories of CubeSats are greatly constrained by limited propulsion capacity. A higher specific impulse, I_{sp}, suggests a higher Δv budget for a given propellant mass. Electric propulsion systems that generally come with high I_{sp} are promising for CubeSats. On the other hand, the generally low thrust of electric propulsion systems may not be applicable for the situation requiring quick maneuvers. Preliminary trajectory design is generally carried out in a simplified dynamical model with a few impulsive maneuvers. However, gravity of celestial bodies can exert positive or negative influence, which can alter the feasibility of low-thrust trajectories. In order to confirm the trajectory feasibility, a refined trajectory analysis should be carried out in the full-ephemeris model and take into account specifications of the CubeSat and selected propulsion system. This section discusses the requirement for deployment trajectories and stationkeeping, which determines suitable propulsion systems and the mission lifetime.

5.1. Deployment trajectories

Four CubeSats should be evenly distributed along the halo orbit to form the favorable geometry. As it is not economical to launch four CubeSats separately, it is assumed that a mother spacecraft takes four CubeSats along with the lander to the Moon. In the transfer phase from the Earth to the halo orbit, the rocket and mother spacecraft can provide the necessary boost.
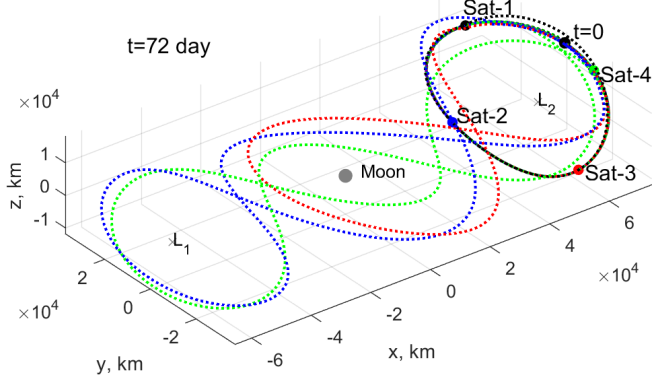
Figure 8: Phasing trajectories (dashed) to deploy four CubeSats evenly along the halo orbit (solid black).

However, it is unrealistic for the mother spacecraft to bring four CubeSats to their different destinations one by one, as the fuel cost be extremely high. Therefore, it is further assumed that the CubeSats as a whole are released at a stable manifold trajectory heading for the halo orbit. Then, the CubeSats are distributed into different phase angles of the halo orbit relying on the propulsion systems on-board.

5.1.1. Deployment trajectory design in the simplified model

A previous work has investigated the phasing trajectory in the CR3BP using two impulses (Chen et al. (2016); Chen and Ma (2017)). Trajectories to distribute four CubeSats evenly along a halo orbit with $A_z = 15,000$ km is shown in Figure 8. Δv and the time of flight (ToF) for each CubeSat are listed in Table 4. The trajectory of Sat-3 requires relatively quick response; that is, gaining a Δv of 101 m/s in a short ToF of 50 days, which can pose a high requirement on the thrust magnitude. The following subsections discusses the trajectory requirement in terms of Δv and thrust magnitude, F_T, for the deployment trajectory of Sat-3.

5.1.2. Solution existence vs thrust magnitude

To gain a quick view of the relation between solution existence and thrust magnitude, a number of optimization runs are performed with different maximum thrusting acceleration, acc_{thr} in the simplified Earth-Moon CR3BP. In

Table 4: Deployment costs

CubeSat	Δv, m/s	ToF, days
Sat-1	55	47
Sat-2	99	62
Sat-3	101	50
Sat-4	42	71

this optimization, continuous-thrust is assumed but the propellant loss is not considered, because no I_{sp} information is involved. The result of Δv vs acc_{thr} is shown in Figure 9. It can be seen that Δv is maintained at a low level where acc_{thr} is high. Δv starts to increase as acc_{thr} is decreased down to 5×10^{-4} m/s^2, and there is no solution where $acc_{thr} < 7.4 \times 10^{-5}$ m/s^2. Recalling the dry mass of the CubeSat, the corresponding minimum F_T is 0.4 mN, which has excluded most models of micro electric propulsion systems. A survey of propulsion systems is carried out to find suitable systems that meet both the Δv and acc_{thr} constraints, taking into account the dry mass of the CubeSat, and F_T, I_{sp}, propellant mass, and dry mass of the propulsion system. Suitable models are listed in Table 5. The cold-gas system occupies larger mass and volume than the electrospray system, but can produce less Δv due to the small I_{sp}. The chemical systems seem to be the best in terms of all indices, but they are considered less stable than cold-gas and electric systems.
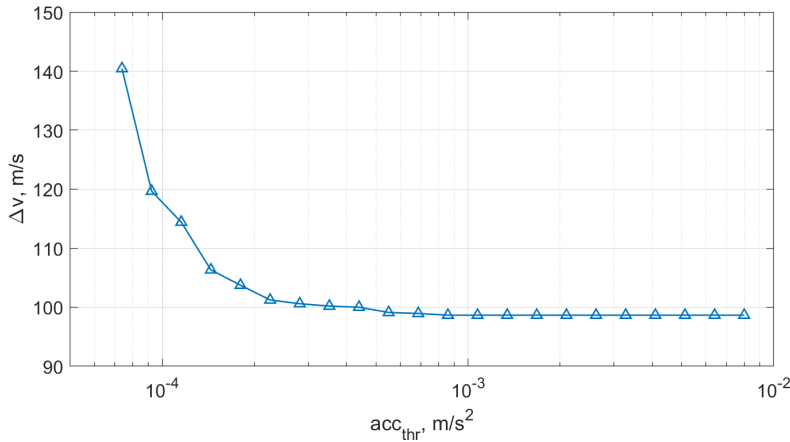
Figure 9: Δv vs acc_{thr}.

5.1.3. Low-thrust trajectory optimization in the high-fidelity model

If the mission uses the electrospray system with a maximum thrust of 0.7 mN, a further effort is made to verify the feasibility of the low-thrust trajectory in the high-fidelity model. The high-fidelity model used in this work takes into account the ephemerides (IMCCE INPOP17a, Viswanathan et al. (2017, 2018)) and gravity of the Sun, Earth, and Moon, and the solar radiation pressure assuming that the reflectivity $C_R = 1.3$ and exposed area $A = 0.1$ m^2. F_T applied on the trajectory is constrained by 0.7 mN. The propellant loss due to thrusting is integrated along the trajectory. The propellant loss rate, $\dot{m}$, is expressed as,

$$\dot{m} = F_T/(I_{sp}g_0) \tag{9}$$

where g_0 is the standard gravity on the Earth.

A parallel high-fidelity optimization tool, PHITO, based on multiple shooting and nonlinear programming methods has been developed for trajectory optimization (for details, see Chen et al. (2018a)). PHITO can scale variables, constraints, and objective function, and integrate segments of trajectories as well as the partial derivatives with respect to initial states and thrusting vectors in parallel. With the partial derivatives, gradients of boundary conditions and objective (i.e. propellant mass) can be easily derived based on chained rule, which facilitate the optimization process (see also Yam and Kawakatsu (2015); Campagnola et al. (2015); Meng et al. (2018); Dei Tos and Topputo (2019)). In PHITO, ephemerides are obtained by the tool CALCEPH (Gastineau et al. (2018)), which can be called in a parallel computing environment . The nonlinear programming software SNOPT (Gill et al. (2005)) is called in PHITO to optimize the problem.

Trajectories starting on different Julian dates that are sampled every 10 days during the period from 2019-2020 are optimized by PHITO. As in the high-fidelity model closed halo orbits do not exist, the boundary conditions are slightly loosen. That is, the boundary x-amplitude of the halo orbit is allowed to vary within a range of 3000 km, and the boundary velocity v_y in the rotating frame is allowed to vary within a range of 10 m/s. The result of Δv is shown in Figure 10. The lunar phase angle (i.e. the true anomaly of the Moon's orbit) is also displayed. Results show that the solution always exists for the low thrust of 0.7 mN regardless of the initial Julian Date. The lowest Δv generally occurs at the lunar phase angle between 205° and 240°, revealing the influence of the lunar ephemeris. The largest difference between the Δv

Table 5: Suitable propulsion systems

Model	Type	Dry, kg	Propel., kg	Power, W	Size, U	Thrust, mN	I_{sp}, s	Δv, m/s
Aerojet MPS-120[1]	Chemical	1.06	0.38	10	1	250	206	142.5
VACCO Hybrid ADN[2]	Chemical	1.01	0.53	14	1	100	200	192.5
JPL MarCo[3]	Cold-gas	1.56	1.93	10	2	50	40	106.5
Busek Bet-1mN[4]	Electrospray	1.07	0.08	15	1	0.7	800	119.6

[1] http://www.rocket.com/cubesat/mps-120, accessed on 19-Nov-2018
[2] https://www.cubesat-propulsion.com/wp-content/uploads/2015/10/adn-micropropulsion-system.pdf, accessed on 19-Nov-2018
[3] https://www.cubesat-propulsion.com/jpl-marco-micro-propulsion-system/, accessed on 19-Nov-2018
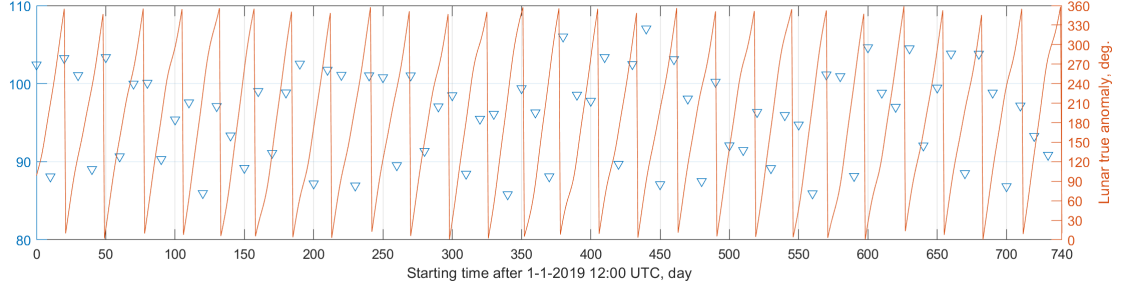[4] http://www.busek.com/technologies_espray.htm, accessed on 19-Nov-2018

Figure 10: Δv for different initial dates.

is 21 m/s. By choosing a favorable mission date, such an amount of Δv can be saved. Nevertheless, Δv does not vary much since the standard deviation is only 6 m/s. The average Δv is 96 m/s. If the trajectory is considered in the simplified CR3BP, the required Δv from Figure 9 is 104 m/s. That means the full-ephemeris n-body dynamics generally bring positive effect on this trajectory. After deployment a Δv budget around 20 m/s is left for stationkeeping. An example trajectory starting on 01-01-2019 is shown in Figure 11. The nominal two-impulsive trajectory obtained in the CR3BP is also shown for comparison. The high-fidelity trajectory deviates from the nominal evidently, especially on the halo-orbit leg.
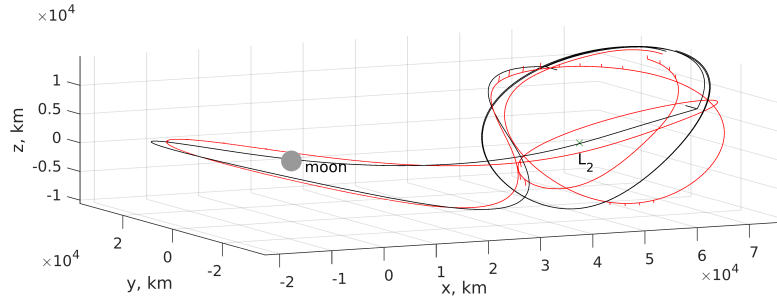

Figure 11: Low-thrust trajectory (red) in the high-fidelity model and nominal two-impulsive trajectory (black) in the Moon-centered rotating frame.

5.2. Stationkeeping

The stationkeeping cost is examined to reveal the mission lifetime. A stationkeeping maneuver is planned at every x-z plane crossing in the rotating
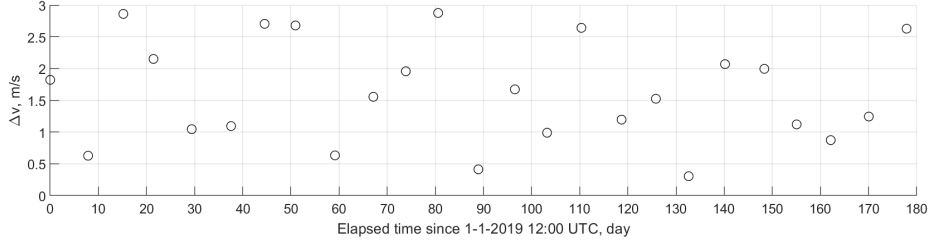
23

Figure 12: Station keeping Δv.

frame. The targeting condition is that the trajectory at the next xz-plane crossing has zero velocity in the x and z directions (Folta et al. (2012)). The time between two crossings is not fixed but loosen to enjoy a Δv optimality. The correction interval is around half a halo period (i.e. 7.4 days). In the simulation, orbit determination errors with 3σ position uncertainty of 200 m and velocity uncertainty of 0.1 cm/s are generated. Figure 12 shows a half-year history of stationkeeping Δv for a simulation starting on 1-1-2019 12:00 UTC, and Figure 13 shows the corresponding maintained halo orbit. The average Δv per maneuver is 1.63 m/s and the standard deviation is 0.8 m/s. The average cost per month is 6.7 m/s. Recalling the deployment Δv in Table 4 and Δv budget in Table 5, if the Busek Bet-1mN system is used, Sat-2 and Sat-3, which have the least Δv margin, can stay in the halo orbit for 2 months after the deployment is accomplished. Nevertheless, the landing mission will have been accomplished before Sat-2 and Sat-3 escape. Sat-1 and Sat-4 can continue to stay another 10 months to provide communication relay, and track lunar users using LiAISON (Hill and Born (2007); Hesar et al. (2015)). If the VACCO Hybrid ADN system is used, the whole system can sustain and keep providing the complete tracking service for 14 months. The MarCo cold-gas system, however, would barely have the Δv budget for stationkeeping after deployment.

6. Conclusion

This paper shows the feasibility of a low-cost lunar far-side positioning mission employing four 3U CubeSats in an EML2 halo orbit. The analysis reveals that a small halo orbit with A_z around 15,000 km is favorable with relatively wide coverage of the lunar surface and good geometry for positioning. The far-side area with longitude between [E125°, W125°] and latitude
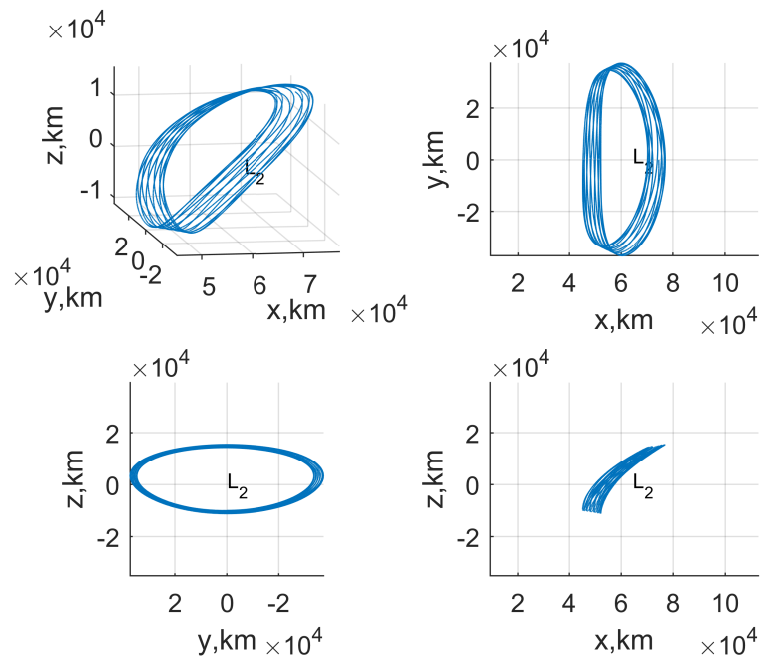
24

Figure 13: The halo orbit maintained by stationkeeping maneuvers.

between [N75°, S75°] is covered. Given a 3σ CubeSat position uncertainty of 200 m, the best achievable accuracy of the lander position is 2.7 km. The best positioning accuracy is associated with the best geometry, which recurs every 3.7 days. The waiting time is considered acceptable for a lunar mission. Moreover, the CubeSat constellation can be exploited to support near real-time orbit determination of lunar orbiters with position accuracy of 16.1 m and velocity accuracy of 1.9 cm/s.

As it is required to distribute four CubeSats evenly along the halo orbit, deployment trajectories along with propulsion systems have been discussed. A low-thrust trajectory optimization is carried out in the high-fidelity model. The result indicates that a thrust as low as 0.7 mN can achieve the required deployment regardless of the initial Julian Date. Several state-of-the-art chemical and electrospray propulsion models are shown suitable in terms of required Δv budget and thrust magnitude for the deployment. Depending on the propulsion system used, the mission lifetime can range from 2 to 14 months considering the stationkeeping cost. Detailed trade-off studies, optimization of subsystems, in-flight power analysis, etc. will be carried out in the future work.

Acknowledgments

Reference

Burns, J. O., Kring, D. A., Hopkins, J. B., Norris, S., Lazio, T. J. W., Kasper, J., 2013. A lunar L2-Farside exploration and science mission concept with the Orion Multi-Purpose Crew Vehicle and a teleoperated lander / rover. Advances in Space Research 52 (2), 306–320.

Campagnola, S., Hernando-Ayuso, J., Kakihara, K., Kawabata, Y., Chikazawa, T., Funase, R., Ozaki, N., Baresi, N., Hashimoto, T., Kawakatsu, Y., Ikenaga, T., Oguri, K., Oshima, K., 2018. Mission Design of the EQUULEUS and OMOTENASHI Cubesats. In: 69th International Astronautical Congress. Bremen, Germany.

Campagnola, S., Ozaki, N., Sugimoto, Y., Yam, C. H., Chen, H., Kawabata, Y., Ogura, S., Sarli, B., Kawakatsu, Y., Funase, R., Nakasuka, S., 2015. Low-Thrust Trajectory Design and Operations of PROCYON, The First Deep-space Micro-spacecraft. In: 66th International Astronautical Congress. Jerusalem, Israel, paper IAC-15,C1,1,8,x28941.

Chen, H., Gastineau, M., Hestroffer, D., Viswanathan, V., 2018a. Parallel High-fidelity Trajectory Optimization with Application to CubeSat Deployment in an Earth-moon Halo Orbit. In: 7th Interplanetary CubeSat Workshop. Paris, France, paper A.1.4.

Chen, H., Liu, J., Long, L., Xu, Z., Hestroffer, D., 2018b. Lunar Far Side Positioning Enabled by a Deployed CubeSat System in an Earth-moon Halo Orbit. In: 42nd COSPAR Scientific Assembly. Pasadena, CA, USA, abstract PSD.1-0029-18.

Chen, H., Liu, L., Meng, Y., Long, L., Xu, Z., Liu, J., 2017. Preliminary Mission Design and Analysis of a Lunar Far-side Positioning CubeSat Mission. In: 26th International Symposium on Space Flight Dynamics. Matsuyama, Japan, paper ISTS–2017–d–160/ISSFD–2017–160.

Chen, H., Ma, J., 2017. Phasing Trajectories to Deploy a Constellation in a Halo Orbit. Journal of Guidance Control, and Dynamics 10 (40), 2662–2667.

Chen, H., Meng, Y., Ma, J., 2016. Phasing Trajectories for a CubeSat Lunar Far-side Positioning Mission. In: Workshop on JAXA Astrodynamics and Flight Mechanics. Sagamihara, Japan.

Cipriano, A., Dei Tos, D., Topputo, F., 2018. Orbit Design for LUMIO: the Lunar Meteoroid Impacts Observer. In: Frontiers in Astronomy and Space Science. pp. 1–23.

Davis, D. C., Bhatt, S. A., Howell, K. C., Jang, J. W., Whitley, R. J., Clark, F. D., Guzzetti, D., Zimovan, E. M., Barton, G. H., 2017. Orbit maintenance and navigation of human spacecraft at cislunar near rectilinear halo orbits. Advances in the Astronautical Sciences 160, 2257–2276.

Dei Tos, D. A., Topputo, F., jan 2019. High-Fidelity Trajectory Optimization with Application to Saddle-Point Transfers. Journal of Guidance, Control, and Dynamics.
URL https://doi.org/10.2514/1.G003838

Doedel, E. J., Paffenroth, R. C., Keller, H. B., Dichmann, D. J., Galán-Vioque, J., Vanderbauwhede, A., 2003. Computation of Periodic Solutions of Conservative Systems with Application to the 3-Body Problem. International Journal of Bifurcation and Chaos 13 (06), 1353–1381.

Folta, D. C., Woodard, M. A., Cosgrove, D., 2012. Stationkeeping of the first Earth-Moon libration orbiters: The artemis mission. Advances in the Astronautical Sciences 142, 1697–1715.

Franzese, V., Lizia Di, P., Topputo, F., 2019. Autonomous Optical Navigation for the Lunar Meteoroid Impacts Observer. Journal of Guidance, Control, and Dynamics.

Frick, A., Castillo-Rogez, J., Johnson, L., Dervan, J., 2014. NEA Scout: A CubeSat Architecture for Near Earth Easteroid (NEA) Exploration. In: Interplanetary Small Satellite Conference. Pasadena, CA, USA.

Gastineau, M., Fienga, A., Laskar, J., Manche, H., 2018. CALCEPH - C language -Release 3.1.0. Tech. rep., Institut de mécanique céleste et de calcul des éphémérides, Observatoire de Paris.

Gill, P. E., Murray, W., Saunders, M. A., 2005. SNOPT: An SQP algorithm for large-scale constrained optimization. SIAM Review 47, 99–131.

Gurfil, P., Herscovitz, J., Pariente, M., 2012. The SAMSON Project - Cluster Flight and Geolocation with Three Autonomous Nano-satellites. In: 26th AIAA/USU Conference on Small Satellites. Salt Lake City, UT, USA, paper SSC12-VII-2.

Hernando-ayuso, J., Campagnola, S., Ikenaga, T., Yamaguchi, T., Ozawa, Y., Sarli, B. V., Takahashi, S., Yam, C. H., 2017. OMOTENASHI Trajectory

Analysis and Design: Landing Phase. In: ISTS 31st Special Issue (Submit). Matsuyama, Japan, paper ISTS-2017-d-050/ISSFD-2019-050.

Hesar, S. G., Parker, J. S., Leonard, J. M., Mcgranaghan, R. M., Born, G. H., 2015. Lunar far side surface navigation using Linked Autonomous Interplanetary Satellite Orbit Navigation (LiAISON). Acta Astronautica 117, 116–129.

Hill, K., Born, G. H., 2007. Autonomous Interplanetary Orbit Determination Using Satellite-to-Satellite Tracking. Journal of Guidance, Control, and Dynamics 30 (3), 679–686.

Howell, K. C., 1984. Three-Dimensional, Periodic, 'Halo' Orbits. Celestial Mechanics 32 (1), 53–71.

Kaplan, E. D., Hegarty, C. J., 2006. Understanding GPS: Principles and Applications. ARTECH HOUSE.

Klesh, A. T., 2014. INSPIRE AND MARCO - TECHNOLOGY DEVELOPMENT FOR THE FIRST DEEP SPACE CUBESATS. In: 41st COSPAR Scientific Assembly. Turkey, abstract B0.1–18–16.

Kuppers, M., Carnelli, I., Galvez, A., Mellab, K., Michel, P., the AIM team, 2015. The Asteroid Impact Mission (AIM). In: European Planetary Science Congress 2015. Vol. 10.

Lai, P. C., Sternberg, D. C., Haw, R. J., Gustafson, E. D., Adell, P. C., Baker, J. D., 2018. Lunar Flashlight CubeSat GNC System Development for Lunar Exploration. In: 69th International Astronautical Congress. Bremen, Germany.

Larson, W. J., Wertz, J. R., 2005. Space Mission Analysis and Design, 3rd Edition. Microcosm Press and Kluwer Academic Publishers, El Segundo, Dordrent, Boston, London, pp. 550–575.

Li, F., Zhange, H., Wu, X., Ma, J., Zhou, W., 2014. THE SCIENTIFIC VALUE AND TECHNICAL CHALLENGE OF CHANG'E-4 LANDING ON THE FAR-SIDE OF THE MOON. In: 41st COSPAR Scientific Assembly. Turkey, abstract B0.1–18–16.

Long, L., Jiangkai, L., Song, H., Li, L., Zhu, L., Chen, H., 2017. Preliminary Design and Testing of a Lunar CubeSat System. In: 5th National Symposium on Space Flight Dynamics. Wenchang, China.

Meng, Y., Zhang, H., Gao, Y., dec 2018. Low-Thrust Minimum-Fuel Trajectory Optimization Using Multiple Shooting Augmented by Analytical Derivatives. Journal of Guidance, Control, and Dynamics.
URL https://doi.org/10.2514/1.G003473

NASA, 2015. SPACE LAUNCH SYSTEM (SLS) SECONDARY PAYLOAD USER'S GUIDE (SPUG). Tech. rep., NASA.
URL https://www.nasa.gov/sites/default/files/sls-secondary_payload_users_guide.docx

Oguri, K., Kakihara, K., Campagnola, S., Ozaki, N., 2017. EQUULEUS Mission Analysis: Design of the Science Orbit Phase. In: International Symposium on Space Flight Dynamics. Matsuyama, Japan.

Oshima, K., Campagnola, S., Yam, C. H., Kayama, Y., 2017. EQUULEUS Mission Analysis: Design of the Transfer Phase. In: International Symposium on Space Flight Dynamics. Matsuyama, Japan, paper ISTS-2017-d-159/ISSFD-2019-159.

Remco, K., 2006. Precise Relative Positioning of Formation Flying Spacecraft Using GPS. Ph.D. thesis, Delft, Delft University of Technology.

Schaire, S., 2017. Near Earth Network (NEN) CubeSat Communications. Tech. rep., NASA, Greenbelt, MD, USA.
URL https://ntrs.nasa.gov/search.jsp?R=20170000974

Speretta, S., Topputo, F., Biggs, J., Di Lizia, P., Massari, M., Mani, K., Dei Tos, D., Ceccherini, S., Franzese, V., Cervone, A., et al., 2018. LUMIO: achieving autonomous operations for Lunar exploration with a CubeSat. In: 2018 SpaceOps Conference. Marseille, France.

Szebehely, V., 1967. THEORY OF ORBITS: The Restricted Problem of Three Bodies. Academic Press, New York, San Francisco, London.

Tardivel, S., Klesh, A. T., Campagnola, S., oct 2017. Technology Enabling Interplanetary Trajectories for Nanospacecraft. Journal of Spacecraft and

Rockets 55 (1), 95–105.
URL https://doi.org/10.2514/1.A33789

Vallado, D. A., 2007. Fundamentals of Astrodynamics and Applications. Microcosm Press and Springer.

Viswanathan, V., Fienga, A., Gastineau, M., Laskar, J., 2017. INPOP17a planetary ephemerides. Tech. rep., Institut de mécanique céleste et de calcul des éphémérides, Observatoire de Paris.

Viswanathan, V., Fienga, A., Minazzoli, O., Bernus, L., Laskar, J., Gastineau, M., 01 2018. The new lunar ephemeris inpop17a and its application to fundamental physics. Monthly Notices of the Royal Astronomical Society 476.

Woodard, M., Cosgrove, D., Morinelli, P., Marchese, J., Owens, B., Folta, D., 2012. Orbit determination of spacecraft in Earth-Moon L1 and L2 libration point orbits. Advances in the Astronautical Sciences 142 (1), 1683–1696.

Yam, C. H., Kawakatsu, Y., 2015. GALLOP: A Low-Thrust Trajectory Optimization Tool for Preliminary and High Fidelity Mission Design. In: 30th International Symposium on Space Technology and Science. Kobe, Japan, paper ISTS 2015-d-49.

Yang, C., Liu, J., Long, L., Song, H., Li, L., Zhu, L., Ye, B., Chen, H., Zhang, H., 2019. The Preliminary Design and Test of the Attitude Control System of Lunar CubeSats. Chinese Space Science and Technology(in Chinese).

Zimovan, E. M., Howell, K. C., Davis, D. C., 2017. Near rectilinear halo orbits and their application in CIS-Lunar space. Advances in the Astronautical Sciences 161, 209–228.